Chapter 6

The Muon Storage Ring Magnet

6.1 Introduction

As emphasized in Chapter 2, the determination of the muon anomaly a_μ requires a precise measurement of the muon spin frequency in a magnetic field ω_a, and an equally precise measurement of the average magnetic field felt by the ensemble of precessing muons, $\langle B \rangle$. We repeat the spin equation given in Eq. 2.14, since it is central to the design of the storage-ring magnet.

$$\vec{\omega}_a = -\frac{Qe}{m}\left[a_\mu \vec{B} + \left(a_\mu - \left(\frac{m}{p}\right)^2\right)\frac{\vec{\beta}\times\vec{E}}{c}\right]. \tag{6.1}$$

As explained in Chapter 2, the need for vertical focusing and exquisite precision on $\langle B \rangle$ requires that: either the muon trajectories be understood at the tens of parts per billion level, and the magnetic field everywhere be known to the same precision; or the field be as uniform as possible and well-measured, along with "reasonable knowledge" of the muon trajectories. This latter solution was first employed at CERN [1] and significantly improved by E821 at Brookhaven [2]. The uniformity goal at BNL was ± 1 ppm when averaged over azimuth, with local variations limited to ≤ 100 ppm.

A photograph of the E821 magnet is shown in Figure 6.1. It is clear from the photo that this "storage ring" is very different from the usual one consisting of lumped elements. This continuous magnet, made up of twelve 30° yoke sections was designed to eliminate the end effects present in lumped magnets, which have large gradients and would make the determination of $\langle B \rangle$ difficult. Furthermore, a small pertubation in the yoke can effect the field halfway around the ring at the ppm level. Thus every effort was made to minimize holes in the yoke, and other pertubations. Thus the only penetrations through the yoke were to permit the muon beam to enter the magnet, and to connect cryogenic services and power to the inflector magnet and to the outer radius coil. Where a hole in the yoke was necessary, extra steel was placed around the hole on the outside of the yoke to compensate for the effect in the magnetic circuit.

Fermilab E989 will use the storage-ring magnet designed and built for Brookhaven E821, with additional shimming to further decrease the local variations in the magnetic field. This requires the relocation of the ring from BNL to Fermilab, which is described in detail in the following chapter. While the magnet steel comes apart and can be moved by conventional

Figure 6.1: The E821 storage-ring magnet at Brookhaven Lab.

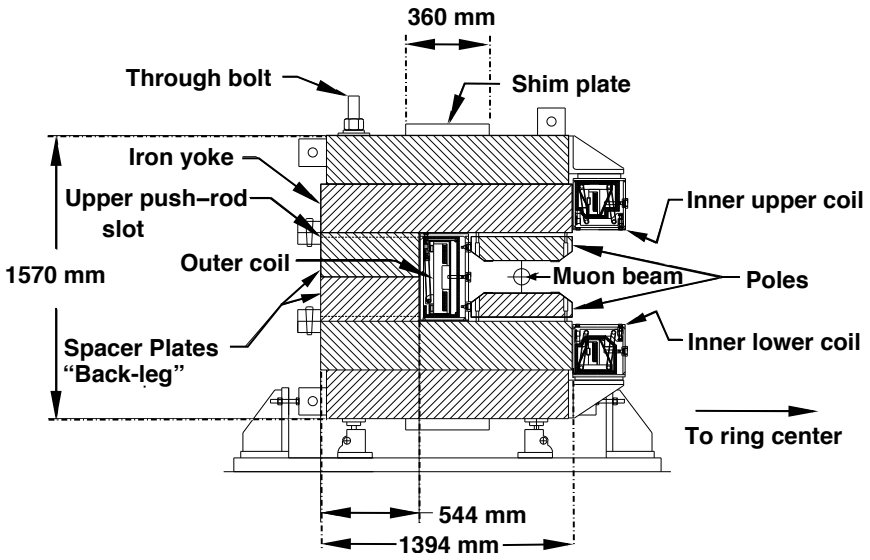

Figure 6.2: Cross section of the E821 storage-ring magnet. The yoke is made up of 12 azimuthal sections, each of which consists of six layers of high quality magnet steel provided by Lukins Steel Corporation. The pole pieces were provided by Nippon Steel Corporation.

trucks, the 14.5 m diameter superconducting coils will need to be moved as a package, on a custom designed fixture that can be pulled by a truck to travel by road, and put on a barge to travel by sea, and then again by road to get it to the Fermilab site.

6.2 Design Considerations

The storage ring is built as one continuous superferric magnet, an iron magnet excited by superconducting coils. A cross-section of the magnet is shown in Fig. 6.2. The magnet is C-shaped as dictated by the experiment requirement that decay electrons be observed inside the ring. The field, and hence its homogeneity and stability, are determined dominantly by the geometry, characteristics, and construction tolerances of the iron. Although both copper and superconducting coils were considered, the use of superconducting coils offered the following advantages: thermal stability once cold; relatively low power requirements; low voltage, and hence use of a low-voltage power supply; high L/R time constant value and hence low ripple currents; and thermal independence of the coils and the iron. The main disadvantage was that the coils would have a much larger diameter and smaller height than any previously built superconducting magnet. However, since the E821 magnet team could not identify any fundamental problems other than sheer size, they decided to build superconducting coils.

To obtain the required precision in such a large diameter magnet with an economical design is an enormous challenge. The magnet had to be a mechanical assembly from sub-pieces because of its size. With practical tolerances on these pieces, variations up to several thousand ppm in the magnetic field could be expected from the assembled magnet. To improve this result by two to three orders of magnitude required a design which was a "shimable kit".

Because of the dominant cost of the yoke iron, it was an economic necessity to minimize the total flux and the yoke cross-section. This led to a narrow pole, which in turn conflicts with producing an ultra-uniform field over the 9 cm good field aperture containing the muon beam.

A simple tapered pole shape was chosen which minimized variations in the iron permeability and field throughout the pole. The ratio of pole tip width to gap aperture is only 2/1. This results in a large dependence of the field shape with the field value B. However, since the storage ring is to be used at only one field, $B = 1.45$ T, this is acceptable. Because of dimensional and material property tolerance variation, the compact pole piece increases the necessity for a simple method of shimming.

Experience with computer codes, in particular with POISSON [4], had demonstrated that, with careful use, agreement with experiment could be expected at a level of 10^{-4} accuracy. POISSON is a two-dimensional (2D) or cylindrically symmetric code, appropriate for the essentially continuous ring magnet chosen for the $(g-2)$ experiment. Computational limitations, finite boundary conditions, and material property variations are all possible limitations on the accuracy of "paper" designs.

We will briefly discuss the design features that are relevant to E989, especially to moving the ring, but not repeat all the details given in Danby et al. [3], and in the E821 Design Report [5]. The parameters of the magnet are given in Table 6.2

6.2.1 The Superconducting Coils

The coil design was based on the TOPAZ solenoid at KEK [6]. TOPAZ conductor was used, with pure aluminum stabilizer and niobium-titanium superconductor in a copper matrix.

Table 6.1: Magnet parameters

Design magnetic field	1.451 T
Design current	5200 A
Equilibrium orbit radius	7112 mm
Muon storage region diameter	90 mm
Inner coil radius - cold	6677 mm
Inner coil radius - warm	6705 mm
Outer coil radius - cold	7512 mm
Outer coil radius - warm	7543 mm
Number of turns	48
Cold mass	6.2 metric tons
Magnet self inductance	0.48 H
Stored energy	6.1 MJ
Helium-cooled lead resistance	6 $\mu\Omega$
Warm lead resistance	0.1 mΩ
Yoke height	157 cm
Yoke width	139 cm
Pole width	56 cm
Iron mass	682 metric tons
Nominal gap between poles	18 cm

Conductor characteristics are given in Table 6.2.1. At full field the critical temperature of the outer coil is 6.0 K. The magnet typically operates at 5.0 K. This represents 76% of the superconductor limit. Each coil block is effectively a very short solenoid with 24 turns, and one layer. The coils are wound from the inside of the ring so that, when powered, the coils push out radially against a massive aluminum mandrel. Cooling is indirect with helium pipes attached to the mandrels. The coil turns, coil stack and insulation are epoxied together, forming a monolithic block. The coils hang from the cryostat with low heat load straps, and the shrinkage and expansion of the coils is taken by the straps. The coils are located using radial stops on the inner radius. For the outer coil the stops transfer the force from the coil to the cryostat box, and push rods from the iron yoke transfer the force from the box to the iron (see Fig. 6.3). For the inner coils, pins replace the pushrods.

When the coils are cooled, they contract down onto the radial stops into a scalloped shape. When powered, the Lorentz force pushes the coils outward, increasing the force against the mandrel, which provides cooling. This feature, the result of winding on the inside of the mandrel, reduces the risk of cooling problems even if the coil were to separate from the mandrel during transport citeyamamoto-pc.

A ground plane insulation band of 0.3 mm thickness was built from a sandwich of three layers of 50 μm kapton, epoxy coated, between two layers of epoxy-filled fiberglass. The insulation assembly was fully cured and placed into the mandrel. A 0.1 mm layer of B-stage epoxy film was placed between the mandrel and kapton laminate, and between the kapton laminate and the conductor block after winding. A 4.8 mm thick G-10 piece was placed on

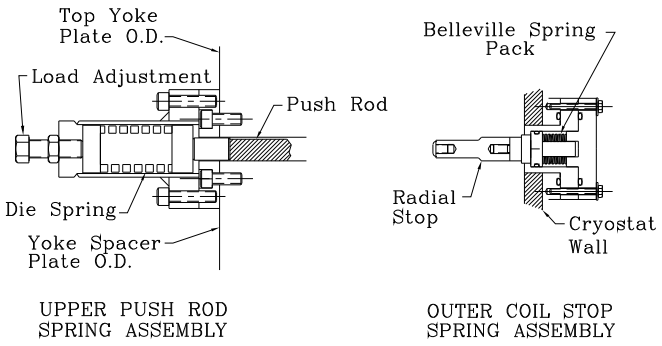

Figure 6.3: The spring-loaded radial stop and push rod. The stops are attached to the cryostat inner wall. The push rods preload the outer cryostat, attaching to the yoke at the outer radius, passing through a radial slot in the yoke to the outer cryostat.

the winding ledge, and on top and on the inner radius of the completed coil block. The insulation protected against a local failure in an insulation layer and against creep failure along a surface. The epoxy-filled fiberglass in the ground plane insulation sandwich improved heat transfer between coil and mandrel.

Table 6.2: Superconductor parameters

Superconductor type	NbTi/Cu
Nominal dimensions	1.8 mm × 3.3 mm
NbTi/Cu ratio	1:1
Filament 50 μm	
Number of filaments	1400
Twist pitch	27 mm
Aluminum stabilizer type	Al extrusion
Ni/Ti composite dimensions	3.6 mm × 18 mm
Al/(NbTi + Cu) ratio	10
RRR (Al)	2000-2500
RRR (Cu)	120-140
I_c	8100 A (2.7 T, 4.2 K)

The coil was then wound using a machine that wrapped the superconductor with three overlapping layers of 25 μm of kapton and fiberglass filled with B-stage epoxy, 19 mm in width, laying the conductor into the mandrel with a compressive load as described in Ref. [3]. The wrap was tested at 2000 V DC during the wind. Aluminum covers were added after the coil was wound, and the entire assembly heated to 125° C to cure the epoxy. See Fig. 6.4.

The outer coil contains two penetrations, one to permit the beam to enter the ring, and one which which could have permitted high voltage to be fed to a proposed electrostatic muon kicker. It was decided at the time to make this "kicker penetration" in the outer coil, but not to make a hole through the magnet yoke until it was shown that this kicker could be built (which was not demonstrated).

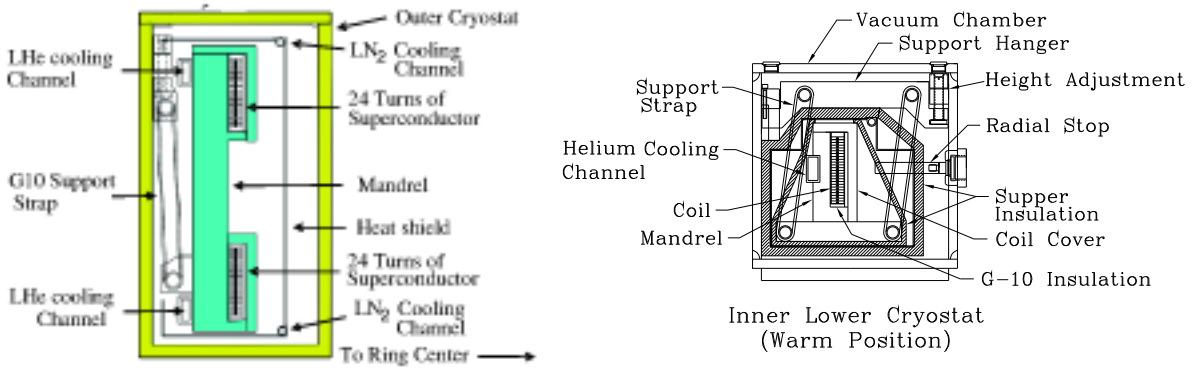

(a) Outer Coil (b) Inner Coil

Figure 6.4: The outer and inner coil structures. Both are shown in their warm configuration.

The coils are indirectly cooled with two-phase He flowing through channels attached to the mandrel, as shown in Fig. 6.4. The two-phase helium cooling avoids the increase in temperature that would occur in a circuit cooled with single-phase helium. The operating temperature of the coils is within 0.2 K of the coldest temperature in the cooling circuit. The advantages of two-phase cooling are: (1) the helium flows in well-defined flow circuits; (2) the total amount of helium that can be flashed off during a quench is limited to the mass of helium in the magnet cooling tubes; and (3) the location of the helium input and output from the cryostat and the location and orientation of the gas cooled leads are not affected by the cooling system [8].

The key to the operation of a two-phase helium cooling circuit is a helium dewar (the control dewar) that contains a heat exchanger. This heat exchanger sub-cools the helium from the J-T circuit before it enters the magnet cooling circuits. This isobaric cooling provides a higher ratio of liquid to gas with a higher pressure and lower temperature than the refrigerator J-T circuit alone would provide. This feature is important for the long cooling channels in the magnet cooling circuits. The use of a heat exchanger in the control dewar reduces the helium flow circuit pressure drop by a factor of two or more. The control dewar and heat exchanger also have the effect of damping out the oscillations often found in two-phase flow circuits. The helium in the control dewar acts as a buffer providing additional cooling during times when the heat load exceeds the capacity of the refrigerator.

The $(g-2)$ cooling system was originally designed to have three separate cooling circuits: a 218 m long cooling circuit that cools all three mandrels in series, the lead and coil interconnect circuits that are 32 m long (the gas-cooled leads are fed off of this circuit), and a 14 m long cooling circuit for the inflector magnet. Later the cooling system was modified to permit each of the mandrels to be cooled separately. Ultimately, the $(g-2)$ cooling system

operates with parallel cooling circuits for the coils, inflector, and lead cooling. Electrically, the three coils are connected in series so that the two inner coils are in opposition to the outer coil to produce a dipole field between the inner and outer coils. The magnet is powered through a pair of tubular gas-cooled leads developed for this application. Each lead consists of a bundle of five tubes. Each tube in the bundle consists of three nested copper tubes with helium flow between the tubes. The copper tubes used in the leads are made from an alloy with a residual resistance ratio of about 64. The lead length is 500 mm. A typical cool down from 300 to 4.9 K takes about 10 d. Once the control dewar starts to accumulate liquid helium, it takes another day to fill the 1000 l dewar. In operation, the pressure drop across the magnet system is about 0.02 MPa (3.0 psi). We initiated several test quenches and had one unintentional quench when the cooling water was shut off to the compressors. The peak measured pressure during a 5200 A quench was 0.82 MPa (105 psig). Other places in the cooling circuit could have a pressure that is 40% higher. The quench pressure peak occurs 11 s after the start of the quench. The quench pressure pulse is about 12 s long compared to current discharge time constant at 5200 A of 31 s. The outer coil mandrel temperature reaches 38 K after the quench is over. Re-cooling of the magnet can commence within 5 min of the start of the quench. After a full current quench, it takes about 2 h for the outer coil to become completely superconducting. The inner coils recover more quickly.

Table 6.3: Estimates of cryogenic heat leaks

		4.9 K load (W)	80 K load (W)
Magnet system heat load	Outer coil cryostat	52	72
	Two inner coils	108	77
	Inflector	8	5
	Interconnects	11	46
	Magnet subtotal	**179**	**200**
Distribution	Helium piping	19	
	Control dewar	5	
	Interconnects/valves	33	32
	Nitrogen piping		34
	Distribution subtotal	**57**	**66**
Lead gas (1.1 g/s)	Equivalent refrigeration	114	
Total refrigeration		351	266
Contingency		70	51
Cryogenic design	**Operating point**	**421**	**308**

6.2.2 The Yoke Steel

The magnet is constructed with twelve 30° sectors, to limit the size and weight of the individual parts for ease of fabrication and assembly. Each sector, Fig. 6.2, is built up of steel plate and consists of an upper and lower yoke separated by a spacer plate. The sector

mass is about 57,000 kg, including end supports and additional parts, and the complete magnet weighs approximately 680 metric tons.

It is difficult to find suppliers of quality steel who can roll plate steel to the thickness required for the upper and lower yoke plates. To allow the maximum number of steel suppliers to bid, and to reduce the chances of voids through reduction in thickness during the hot-rolling process, these components have been supplied as two separate plates. The plates were welded together at the interface during the machining step. The spacer plate is also made in two pieces to facilitate installation of beam pipes, transfer lines and electrical connections to the outer coil cryostat.

The upper and lower yoke plates and spacer plates are held in place by eight high-strength steel bolts per sector, extending through all of the plates vertically. These bolts are 5 cm in diameter and were tensioned to 80,000 kg each, which is 57% of the yield point. In addition, the three assemblies, the upper yoke plate, spacer plate and lower yoke plate are doweled together to allow ease of disassembly and reassembly while maintaining their horizontal relationship.

A feature of the overall magnetic design is to have the yoke continuous azimuthally. To achieve this, each sector end has four radial projections for bolts to fasten adjacent sector ends to each other. When the sectors are fitted to each other, shimmed, and the bolts tightened, relative motion of adjacent sectors is minimized.

Rolled steel plates are specified for the major pieces of steel used in the yoke plates and spacer plates. These have 0.08% carbon maximum with a minimum of alloying elements and impurities. All rolled plates have been completely inspected ultrasonically for voids and the composition of each plate has been determined by chemical analysis. The background information of each piece was retained by a numbering system stamped into the steel pieces.

The lower horizontal face of the upper yoke plate and the upper horizontal face of the lower yoke plate were milled flat within 130 μm and 1.6 μm finish. The inner radius of each yoke plate machining tolerance was to within $\pm$130 μm of the basic dimension.

Upper and lower surfaces of the spacer plate were milled flat within $\pm$130 μm and parallel within 180 μm, and thickness accurate to $\pm$130 μm. Both inner and outer radii of the spacer plate tolerances were within $\pm$130 μm of the true radius. The as-built vertical yoke gap has an rms deviation of $\pm$90 μm, or 500 ppm of the total air gap of 20 cm, and a full-width spread of $\pm$200 μm.

Azimuthally machining requirements were that the sector ends be perpendicular to the gap faces to within $\pm$0.3 mrad and that the ends be radial to within $\pm$0.2 mrad. The chords between the outer radius corners of the as-machined sectors have an rms deviation of $\pm$0.25 mm and a mean of -0.03 mm. The design azimuthal gap between sectors was 0.5 mm. The as-built azimuthal gaps for the lower yoke average 0.8 mm, with an rms deviation of $\pm$0.2 mm. Spacer plates and upper sectors were matched to the lower sectors to equalize the effective azimuthal gap for the three pieces, weighted by the magnetic reluctance for each sector.

The magnet is intended to move as a single rigid body, as much as possible. The magnet supports are located at the 12 sector joints, and are designed to move the sector pairs together. The ring also sits on low-friction pads, and is held to the floor at only one azimuthal position.

6.2.3 The Pole Pieces and Wedges

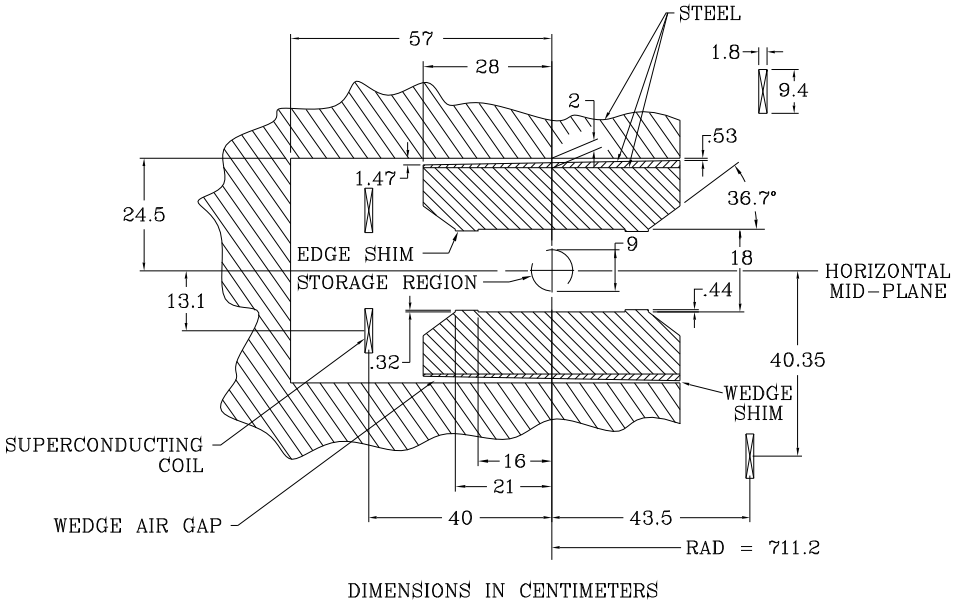

Figure 6.5: Cross section view of the magnet gap region.

The pole pieces are shown in Figs. 6.2 and 6.5. Fig. 6.6 shows the inflector exit and beam vacuum chamber between the poles. The poles directly affect the field quality, while the effect of yoke imperfections is minimized by the air gaps between the yoke and poles. The poles require high-quality steel, with tight machining tolerances on the flatness of the faces which define the storage ring gap. The pole steel was continuous vacuumcast with 0.004% carbon. The tolerance on flatness was 25 μm, which represents 140 ppm of the storage gap. The surface was ground to a 0.8 μm finish (4 ppm). The pole widths were machined to 56 $\pm$0.005 cm, and the thickness to 13.3 $\pm$0.004 cm. The upper and lower faces were machined parallel to 0.005 cm.

In order to control and adjust the pole location and tilt, the poles were constructed in 10° azimuthal sections, compared to the 30° sectors of the yoke. The pole edges that align with the yoke sectors were machined radial, and the middle pole of each sector is interlocking, with a 7° angle from radial. The poles were located azimuthally with 80 μm kapton shims, with the pole edge each 60° in azimuth machined to the correct azimuth. Then kapton was used to electrically isolate the poles from each other to control eddy current effects from field changes, from ramping or quench.

The pole edge-shims were built oversized (4.4 mm thick for the shims on the i.d.; 3.2 mm thick for the o.d. shims) to allow for perturbation adjustment during the magnetic field

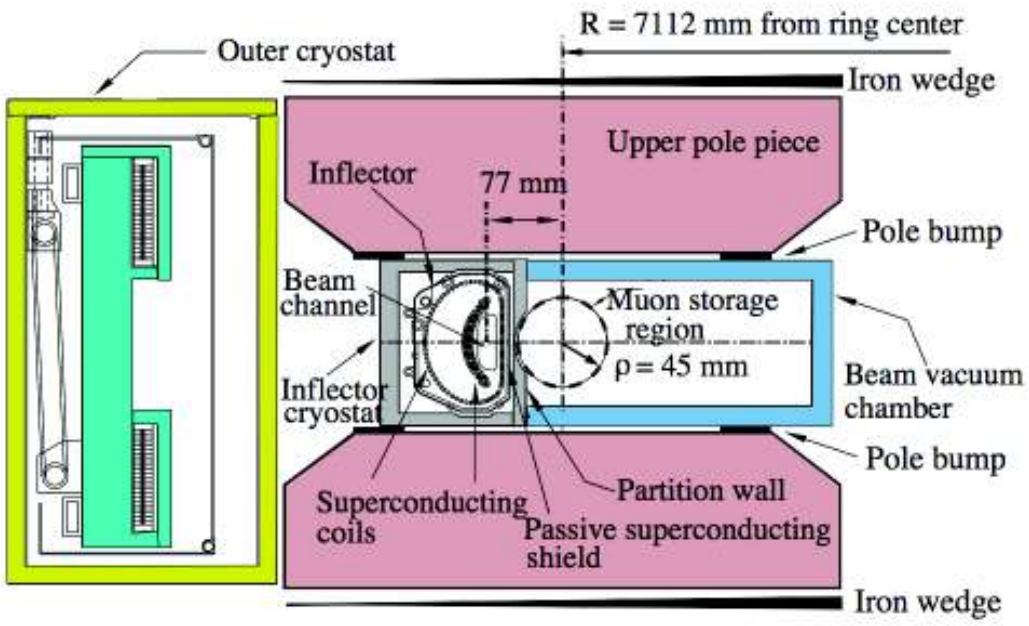

Figure 6.6: The arrangement of the pole pieces, shimming wedges and the inflector cryostat, showing the downstream end of the inflector where the beam exits. The beam is going into the page, and the ring center is to the right.

shimming. The shim width is 5.0 cm. The edge shims are attached to the poles using flathead iron screws, countersunk into the shims every 12 cm in azimuth. This spacing adequately holds the shims from the unstable magnetic force which attempts to short the gap.

The poles are attached to the yoke plates by steel bolts whose heads are counter-bored deeply into the poles (see Fig. 2). The bolts are located in the tapered region of the poles away from the storage region, and the bolt heads are covered by cylindrical plugs of pole steel.

The as-built storage ring gap with a design value of 18 cm was measured using capacitance devices to ± 1 μm accuracy. The gap height varied by ± 23 μm rms with a full range of 130 μm. The tilts of the poles in the radial direction were measured with a precise bubble level and adjusted to ± 50 μrad. The poles were aligned to be horizontal when powered. This required an initial opening angle of 80 μrad toward the ring center to compensate for the asymmetric closing of the gap, as shown in Fig. 6.7(a). Adjacent poles were matched to ± 10 μm to keep field distortions caused by steps in the iron surface small.

The shimming gaps between the yoke and poles serve three purposes: the gaps decouple the yoke steel from the poles; flat dipole correction coils for each pole are installed in the gaps to adjust the dipole field in azimuth; and the gaps contain iron wedges used to shim the magnetic field. The wedges, sloped radially to provide the C-magnet quadrupole correction, are attached so that they can be adjusted radially. The radial adjustment changes the dipole field locally. The wedges are 9.86 cm wide (azimuthal direction), with 72 per 30° sector. They are 1.65 cm thick on the inner radius, 0.5 cm thick on the outer radius, and are 53 cm long (radial direction). Note that the wedges are rectangular in the $r - \phi$ plane, so that there is

a larger gap azimuthally between the wedges on the outer radius.

A difficulty that we did not anticipate was that the magnetic force direction was quite different at lower field than for full field. The wedge angle is designed to distribute the field lines uniformly radially at full field, with the yoke and wedge iron partly saturated. At lower field, however, the iron is not saturated, and the smaller total gap at the larger radius, where the wedges are thicker, draws more field lines. This leads to a torque on the poles and wedges. To stabilize the wedges, clamps were made from aluminum sheets taped together with the appropriate "anti-wedge" shape. The poles are held in place by the bolts described above, and aluminum/steel laminated spacers are used to hold the poles away from the yokes. At full power the force is 2×10^6 N per pole. The iron lamination in the spacers replaces iron in the wedges that are notched, due to the spacers. There are 24 spacers for each 30° sector, located at the sector ends and at 2.5° azimuthal intervals, on the inner and outer radii of the poles. We measured the torque on a pole during ramp-up (Fig. 6.7(b)) and confirmed calculations that the pole attachments were sufficient.

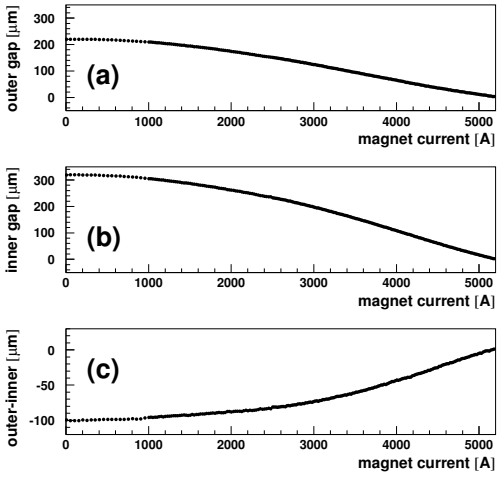

(a) Magnet Gap

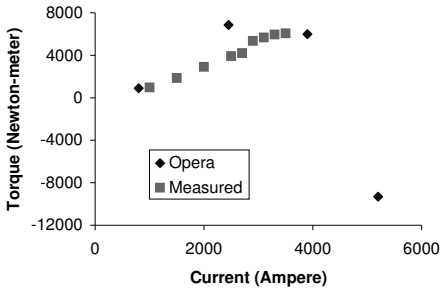

(b) Torque

Figure 6.7: (a)The measurement of the storage ring gap as a function of magnet current, using the capacitance device described in the text. The gap was measured at $r = +15$ cm (a), and $r = -15$ cm (b), relative to the center of the storage region. The gap values at full field, 5200 A, have been subtracted. The total gap closure as well as the difference (a)-(b)=(c) is in good agreement with stress calculations. (b)The measured and calculated torque on a pole during ramp-up, with the pole pivoting about the inner radius spacers. At lower current, the outer radius of the pole tries to short the gap, pulling away from the yoke. The torque at full current, 5200 A, is the opposite sign, with the pole pushing against the spacers toward the yoke.

Another issue that was not appreciated in the design can be understood from Figs. reffg:ring-elevation and 6.6, which has been given the name "the cold cryostat problem". If the vacuum in the outer-diameter cryostat were to become bad, from a liquid helium, liquid nitrogen or

vacuum leak in the cryogenic system, the cryostat will become cold and shrink radially. Given the close proximity of the pole pieces to the cryostat, serious damage could be done to the magnet if such a vacuum failure goes undetected. If a catastrophic loss of vacuum were to occur, the proceedure was to turn off the LHe as quickly as possible and turn on the Roots Blower and the mechanical vacuum pump at U11. The Fermilab experiment will need to develop a plan on how to mitigate the effects of such an incident.

6.3 Power Supply and Quench Protection

Both persistent mode and power supply excitation were considered. The total flux, $\int \vec{B} \cdot d\vec{s}$, is conserved in persistent mode. However, room temperature changes would result in changes in the effective area. Thus although the flux, is conserved, the magnetic field in the muon storage region is not. Persistent mode would also require a high-current superconducting switch. Power supply excitation with NMR feedback was chosen, although no feedback was used for the 1997 run. This method gives excellent control of the magnetic field and allows the magnet to be turned off and on easily. The power supply parameters are shown in Table 6.3.

Table 6.4: Power supply parameters

Rating	5 V, 6500 A	
Rectifier	480 VAC input, 12 pulse (Two $\pm 15°$, 6 pulse units in parallel)	
Output filter	0.4 F	
Regulator	Low-level system	0.1 ppm stability with 17 bit resolution
	Power section	Series regulator with 504 pass transistors
Cooling	Closed loop water system with temperature regulation	
Regulation	Current-internal DCCT	± 0.3 ppm over minutes to several hours
	Field-NMR feedback (current vernier)	± 0.1 ppm (limited by the electronics noise floor)
Manufacturer	Bruker, Germany	

Both persistent mode and power supply excitation were considered. The total flux, $\int \vec{B} \cdot d\vec{s}$, is conserved in persistent mode. However, room temperature changes would result in changes in the effective area. Thus although the flux, is conserved, the magnetic field in the muon storage region is not. Persistent mode would also require a high-current superconducting switch. Power supply excitation with NMR feedback was chosen, although no feedback was used for the 1997 run. This method gives excellent control of the magnetic

field and allows the magnet to be turned off and on easily. The power supply parameters are shown in Table 6.3.

The quench protection design parameters were determined by the requirements of magnetic field stability and protection of the magnet system in case of a quench. When the energy is extracted, eddy currents are set up in the iron which oppose the collapse of the field. This can cause a permanent change in the magnetic field distribution [9]. This is sometimes called the 'umbrellaa effect, since the shape of the change over a pole resembles an umbrella. The eddy currents are minimized if the energy is extracted slowly. There will also be eddy currents in the aluminum mandrels supporting the coils. Electrically, this can be represented by a one turn shorted transformer. These eddy currents will heat the mandrels and can cause the entire coil to become normal. This is called quench-back. This has several beneficial effects. The part of the stored energy that is deposited in the coil is deposited uniformly over the entire coil and mandrel assembly. Also, once quench-back occurs, the energy extraction process is dominated by the quenchback and not by the specifics of where the quench occurred. Therefore, the effects of a quench on the reproducablility of the magnetic field should be minimal.

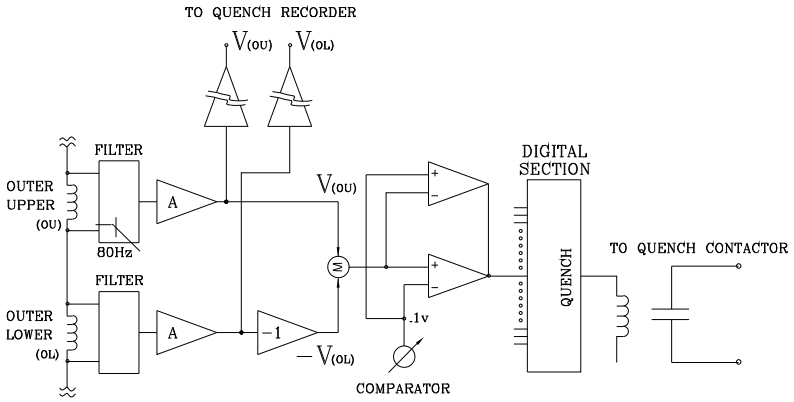

Figure 6.8: Diagram of the quench protection circuit.

The energy extraction system consists of a switch, resistor, and quench detection electronics. An energy extraction resistor of 8 m) was chosen. Including the resistor leads, the room temperature resistance is 8.8 m). This gives an /R time constant of 1 min. The actual time constant varies due to the temperature increase of the coil and dump resistor and the effect of eddy currents in the mandrels during the energy extraction (see below).

This resistance value was calculated to cause quenchback in the outer mandrel within 2 s at full current. The quench protection circuit is shown in Fig. 6.8. The energy extraction trigger for a quench which originates in one of the coils is the voltage difference between matching coils; for example, $V(\text{outer} - \text{upper}) - V(\text{outer} - \text{lower})$. Since the inductance is effectively the same, the voltages should be equal even while charging the magnet, unless a quench develops in one coil. This quench threshold is set at 0.1 V. However, the coil interconnects are thermally coupled together with the helium tubes. It is possible that a quench in an interconnect could propagate to both coils almost simultaneously. Therefore, a voltage threshold of 10 mV was chosen for each interconnect. The outer upper to lower interconnect is only 1 m long. This threshold was set to 5 mV. The thresholds were determined by the requirement that the quench be detected within 0.2 s. The gas-cooled leads develop a voltage of typically 15 mV at full current. If the lead voltage exceeds 30 mV, the energy is extracted.

6.4 Shimming the Magnet

The removable edge shims on the pole surfaces play amajor role in the design of the magnet and its eventual actual shimming corrections. As seen in Fig. 3, the edge shims are symmetrically located about the aperture center line. Various symmetric perturbations of the shims produce predictable multipoles. For example, changing equally all four corners produces only sextupole series terms, proportional to even powers of the aperture radius. Increasing the two outside shims and/or decreasing the inside shims produce only normal quadrupole series terms, proportional to odd powers of the aperture radius. This can be extended to up-down and diagonal (skew) asymmetries. These mathematically predictable asymmetries were indeed found to apply to very high accuracy, including linear superpositions for finite permeability, again showing internal consistency in the computations. Finite and realistic permeability was then used, and the amplitudes of the corner shim perturbations were progressively raised. It was found that the multipole description was still correct and increased linearly with amplitude until unrealistically strong edge shims finally gave a breakdown in linearity as well as in the required symmetries. This gave confidence that the computer calculations could be used to get the design optimization on paper, and also to calculate multipole perturbations of the operating magnet, to correct the field to approaching a 1 ppm level.

Wedge-shaped air gaps between the poles and yoke are an important design feature. These air gaps sufficiently isolate the precision poles from the yoke return that field aberations, or multipoles above the dipole term, are minimally affected by reasonable variations in the yoke reluctance (Table 1). Since the poles dominate the field aberations, the highest quality of iron is only required for the poles. Very pure continuous cast steel is used for the poles. This material is typically of 0.004% carbon content. The higher purity increases permeability at the operating field of the magnet compared to conventional AISI 1006 iron (0.07% carbon typically), which is used for the yoke. Even more important is the impact of the purity on inclusions of ferritic or other extraneous material, air bubbles, etc., which are greatly minimized.

This isolation of field aberations from dipole reluctance has an additional very important property. It is necessary to have large holes through the yoke to inject the beam, for inflector

power and cryogens, and for the outer coil leads and cooling. Because of the isolation from the air gaps, no significant effect on multipoles is observed after restoring the reluctance in the region of the holes by adding large iron collars [5].

The air gaps are wedge-shaped, with a larger air gap on the outer radius, closest to the iron return of the C magnet. The slope is calculated to compensate for the gradient due to C magnet asymmetry (Fig. 2), where the field lines would otherwise tend to cross the gap near the return. Calculations showed that a change in wedge angle caused a very pure normal quadrupole adjustment without inducing higher multipoles. A change in the wedge slope by 1 mm over the length of the wedge changes the quadrupole (at 4.5 cm, the edge of the storage volume) by 15 ppm, while the sextupole term changes by 1 ppm, and the higher multipole changes are still smaller. Attempting to make a large quadrupole adjustment by using pole edge shims introduces octupole, roughly half the size of the quadrupole change [5]. Instead, a combination of wedge angle and inside-outside asymmetry in edge shims can null both quadrupole and octupole.

The inner radius coils, required to be away from the midplane to allow observation of decay electrons from the stored muons, were pulled still further vertically away from the midplane in order to have access to the air gaps for shimming. This has the additional advantage of making the hoop force on these large diameter slender inner coils approximately zero.

The final coil design used a single layer of the KEK TOPAZ pure aluminum stabilized superconductor [6] to excite the 20 cm air gap. The iron circuit dominates so strongly that tolerances on coil location are quite reasonable, as discussed below.

Final pole design involved refinements to the edge shims plus adjustments of the location and angle of the taper of the edges of the poles. To first order, to flatten the field, the cross-sectional area of the edge shims is the important parameter. However, in detail the distance of the inner edge of the shims to the center (Fig. 3), chosen to be rfi16 cm, and the shim width of r"5 cm, optimized the field quality by reducing the r6 multipole. This in combination with an edge angle of 36.7° produced a very small r2 sextupole, the r4 term was nulled, and all higher multipole terms were virtually eliminated.

Making the wedge separate from the poles presented some mechanical complications, but resulted in substantial shimming advantages. A change in the air gap, changing the wedge thickness with no change in angle, produces a very strong effect on the local dipole field, essentially proportional to the thickness change divided by the half-gap of 10 cm. This is because the storage ring aperture and air gaps at the base of each pole constitute 93% of the circuit reluctance. However, small vertical movements of the poles have a small effect on the reluctance, since the combined air gap is unchanged (Table 1).

Errors in the precision pole thickness are small compared to the expected variation of up to 200 μm in the distance between the top and bottom yoke plate surfaces adjacent to the poles.

A means of shimming in the air gaps is attractive, since only dipole is affected, and not higher multipoles. The average thickness of the wedges determines dipole, and the wedge angle determines quadrupole, both essentially pure moments. Finally, if the wedges are radially adjustable, a very fine control for dipole exists. Since the wedge angles are approximately 1 50, radial movement by 50 μm changes the gap by 1 μm, finer control than is available otherwise.

At least on paper, and using realistic parameters, a magnet aperture of 9 cm diameter was designed with a uniform field to a ppm level (Fig. 4). Long-wavelength "real world" errors will be greatest for low-order moments, both normal (field vertical on the horizontal midplane) and skew. The shimming techniques described are designed to correct most of these, with surface coils required to correct skew dipole.

Correcting coils on the surface of the poles permit ultimate fine control of static, and slowly varying errors. The surface coils can be used to correct lowest multipoles to tens of ppm, thus providing significant overlap between the iron shimming and the dynamic shimming. These coils have been constructed to generate moments over the entire 360° azimuth. The coils were designed with printed circuit boards, with 2]120 wires running azimuthally around the ring on the top and bottom pole surfaces facing the storage ring gap, and spaced radially 2.5 mm apart, to avoid lumpy effects which generate higher multipoles. Pole surface corrections can be (and have been) added with ferromagnetic material to correct for local effects in the iron geometry. Local current loops may also be used. The 'continuousa ring was built with 10° pole sections, 36 of which form an almost continuous ring. Dipole correction coils are located in the air gaps for each 10° pole.

Strictly speaking, the description of the storage ring field aberations by multipoles assumes no gradients in the beam direction. However, the muon betatron wavelengths are very long so that longitudinal averaging of actual field data is correct to a very good approximation. For example, for a 10° pole section the azimuthal integral of field data can give an average multipole fit to very good accuracy. The pole edge shims or other adjustments can be applied to correct this 10° average.

Computations of a 75 μm crack between the 10° poles show that the dipole field is reduced slightly locally, but the longitudinal integral was independent of both r and y, so the effect was only on the field integral and not on the field aberations. There are limits to averaging out local field irregularities in the poles, one of which is simply that the ability to measure precisely is more difficult with large gradients. Thus, the $(g-2)$ storage ring shimming effort has the goal to make the field as uniform as practical. Fig. 5 shows the magnetic field lines for the design, and the magnet parameters are given in Table 2.

6.5 ES&H, Quality Assurance, Value Management

References

[1] Bailey J, et al. Nucl. Phys. B150:1 (1979).

[2] Bennett GW, et al.(The Muon $(g-2)$ Collaboration) Phys. Rev. D, 73:072003 (2006).

[3] G.T. Danby, et al., Nucl. Inst and Meth. **A 457**, 151 (2001).

[4] Reference Manual for teh POISSON/SUPERFISH group of codes, LANL, LA-UR-87-126.

[5] Design Report, BNL E821, A New Precision Measurement of the Muon $(g-2)$ Value at the level of 0.35 ppm. 3rd edition, D.H. Brown et al. B.L. Roberts Editor, March 1995.

[6] A. Yamamoto, H. Inoue, H. Hirabayashi, J. Phys. 45 (1984) C1-337.

[7] A. Yamamoto, private communication.

[8] M.A. Green et al., Operation of a two-phase cooling system on a large superconducting magnet, Proceeding of the Eighth International Cryogenic Engineering Conference, Genoa, Italy, June 1980, IPC Science and Technology Press, 1980, p. 72.